NUMERICAL SIMULATION OF AN OSCILLATING AND FLEXIBLE AIRFOIL FOR FLAPPING WING PROPULSION WITH FLUID-STRUCTURE INTERACTION

Ralf Unger, Matthias C. Haupt, Peter Horst
***Institute of Aircraft Design and Lightweight Structures**
Technical University Braunschweig
Hermann-Blenk-Str. 35
38108 Braunschweig, Germany

Keywords: *Lagrange Multipliers, Aeroelasticity, Coupled Problems, Variational Methods*

Abstract

To investigate the aeroelastic effects of a flexible and oscillating airfoil, the numerical analysis of such lightweight structures is described in this contribution. Due to the interaction of the fluid flow with the structural system, a multiphysical approach is employed here, were the jig-shape of the airfoil needs to be calculated. Further, the analysis of low-Reynolds-number flows past this flexible and flapping airfoil is presented where transition from laminar to turbulent flow takes place along a laminar separation bubble. To predict the point of transition, a linear stability solver fully coupled to an unsteady Reynolds-averaged Navier-Stokes flow analysis code is utilized. Results of the simulation of the airfoil's flapping motion in air are presented for specific parameters and discussed in detail.

1 Introduction

To extend the area of application for future micro air vehicles (MAV), the flight speed range needs to be increased. The flapping wing flight inspired by birds locomotion is one way to reach this demand. Both necessary flight forces - lift and thrust - are generated by pitching-plunging mechanism. Here, for simplification a two-dimensional airfoil is investigated first and the question arises if flexibility of such an airfoil is advantageous for the propulsion efficiency. In this paper this issue is addressed and further, the aerodynamics of flapping wing propulsion is still not adequately understood and needs to be investigated.

The size of the MAVs airfoil and the low flight speed range cause a low-Reynolds-number flow regime. The accurate prediction of the flow behavior using computational fluid dynamics (CFD) is still challenging due to the occurrence of laminar-turbulent transition [1, 2, 3, 4]. This transition takes place along a laminar separation bubble, which is caused by a strong adverse pressure gradient within the laminar boundary layer and along the smooth aerodynamic surface. The evolution of the flow from laminar to turbulent proceeds in three stages [2]. In the first, receptivity stage, external disturbances like free stream turbulence or acoustic waves are transformed into low disturbances with wave characteristics within the boundary layer. In the second stage, a small number of unstable waves (Tollmien-Schlichting waves) are amplified and grow exponentially. Their behavior can be mathematically described by the linear stability theory [5]. In the third stage, the amplitudes of the waves increase and a nonlinear interaction with the boundary layer occurs. Thereby, the mean boundary layer profile distorts and the laminar boundary layer breaks down to turbulence.

For the simulation of such flow phenomena fully coupled with a flexible thin structure, a high qualitative and time resolved coupling schemes nowadays used for fluid-structure interaction problems is utilized [6]. The so-called partitioned coupling approach uses well-validated fluid as well as structural solvers, which are linked together within a simulation environment by the aid of flexible data transfer libraries [7]. Four coupling aspects need to be addressed; 1) the data transfer across non-matching interface grids, 2) the time integration and equilibrium iteration of the whole coupled system, 3) the grid deformation of the fluid grid to take the updated geometry into account and 4) the unsteady transition location which needs to be adapted for each deformed fluid grid. For the first aspect, a conservative data transfer scheme based on Lagrange multipliers and the Galerkin discretization is developed. To save computational costs, predictors for the next structural displacements [8] are used for the second aspect. For the third aspect the whole fluid grid is treated as a pseudo structural finite element system, where the current boundary displacements are applied as inhomogeneous boundary conditions.

For the structural part of the simulation environment, a nonlinear finite element methodology is employed [9, 10]. The first eigenfrequency of the structural model is validated against the designed model for the wind tunnel test campaigns [11]. For the fluid part of the simulation environment, an unsteady Reynolds-averaged Navier-Stokes (URANS) flow solver [12] is modified to take the transition process into account [3]. Therefore, for the second stage of the transition process, a linear stability solver [13] is directly coupled to the flow solver to investigate the flow field and especially the boundary layer of the airfoil. The transition location on the upper and lower side of the airfoil is calculated by comparison of a critical N-factor to the N-factor computed by the e^N-method [14, 15]. Due to the use of a URANS solver the first stage is empirically considered by a calibration of the critical N-factor. Further it is assumed that the third stage is very short and that therefore the location of the breakdown to turbulence is equal to the end of the second stage [2].

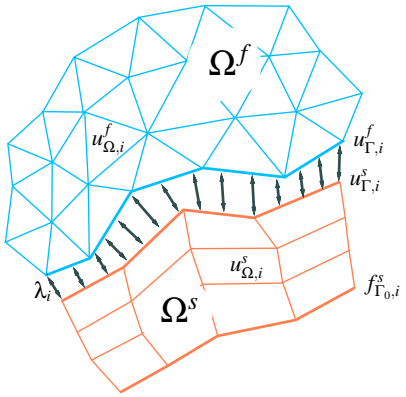

Figure 1: Coupled computational domains

The numerical setup for the coupled system to simulate an oscillating and flexible airfoil for flapping wing propulsion is presented in this paper. This includes the partitioned coupling approach as well as the transition prediction method. Results from unsteady aeroelastic analyses for specific test cases are presented and discussed in detail.

2 Numerical Elements

Due to the nonlinearities, the physical system, where the structure is fully coupled with the flow field, is treated in the time domain. Using a well validated finite element analysis tool for the structure and a finite volume code for the fluid, several coupling aspects have to be considered for the steady and unsteady flight case. The basic partitioned coupling approach is nowadays widely used for Computational Aeroelasticity [16] and some of the numerical elements used and added in this work are discussed in the next subsections.

2.1 Data Transfer

In general, the data transfer takes place across nonmatching interface grids. In Fig. 1, a schematic view of the spatial grid coupling is shown. The structural domain is deformed with discrete values $u^s_{\Omega,i}$ under the boundary loads $f^s_{\Gamma_0,i}$ and λ_i. The structural deformation $u^s_{\Gamma,i}$

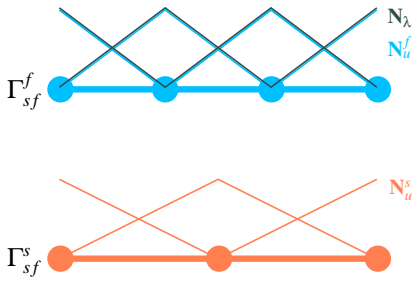

(a) Galerkin based transfer

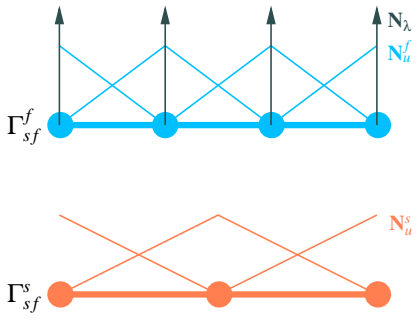

(b) Transfer based on Dirac delta functions

Figure 2: Transfer schemes

on the common interface Γ influences the fluid boundary deformation $u_{\Gamma,i}^f$ and new locations of the fluid grid nodes are evaluated with the aid of $u_{\Omega,i}^f$. The new fluid grid finally leads to updated values for λ_i. Here a weak formulation of the continuity transfer condition is used:

$$u_\Gamma^s = u_\Gamma^f \;\rightarrow\; \int_\Gamma \lambda(u_\Gamma^s - u_\Gamma^f)\,\mathrm{d}\Gamma = 0\,, \qquad (1)$$

where u_Γ^s and u_Γ^f are the structural and fluid displacements defined on the coupling interface Γ, and λ is the Lagrange multiplier, which weights the jump of the interface state variables. The Lagrange multiplier has the physical meaning of a traction force gluing both subdomains together.

By using shape function for the discrete interface state variables, $u_\Gamma^i = \mathbf{N}_u^i \mathbf{u}_\Gamma^i$, the Lagrange multiplier needs to be discretized in a way that the resulting scheme is unique solveable for the nodal values of the fluid interface displacements $\mathbf{u}_\Gamma^f$. This can be carried out by the Galerkin method, where the shape functions of the Lagrange multiplier are chosen to be the same as for the displacements of the fluid interface, $\mathbf{N}_\lambda = \mathbf{N}_u^f$ and Fig. 2a. The discretized version of Eq. (1) then reads:

$$\mathbf{M}_{ff}\,\mathbf{u}_\Gamma^f = \mathbf{M}_{fs}\,\mathbf{u}_\Gamma^s \text{ with } \mathbf{M}_{fi} = \int_\Gamma \mathbf{N}_u^{fT}\mathbf{N}_u^i\,\mathrm{d}\Gamma\,, \qquad (2)$$

which has to be solved for $\mathbf{u}_\Gamma^f$. The coupling matrices $\mathbf{M}_{ff}$ and $\mathbf{M}_{fs}$ are evaluated with the aid of a quadrature rule [6].

Alternatively, a collocation method can be used, where the Dirac-delta function serves as the shape function for the Lagrange multiplier, Fig. 2b. While the latter method is advantageous, because the integral of Eq. (1) vanishes and the transfer equation reduces to the evaluation of the structural shape functions at the fluid nodes, the former shows more local accuracy of the transfer condition [6].

From a given state transfer, the corresponding load transfer is obtained in a straightforward manner by using the transposed relation of the state transfer. According to the principle of virtual work and with the schemes described above, conservation in the load is retained, which is essential for aeroelastic problems. With:

$$\delta\mathbf{u}_\Gamma^{fT}\,\mathbf{f}_\Gamma^f = \delta\mathbf{u}_\Gamma^{sT}\,\mathbf{f}_\Gamma^s \text{ and } \mathbf{u}_\Gamma^f = \mathcal{T}\,\mathbf{u}_\Gamma^s \qquad (3)$$

the load transfer is obtained as:

$$\mathbf{f}_\Gamma^s = \mathcal{T}^T\mathbf{f}_\Gamma^f, \qquad (4)$$

where $\mathcal{T}$ is an operator which maps one variable from one grid to another. Neglecting the forces due to friction of the fluid flow and using the Galerkin based transfer, the fluid pressure distribution can directly be used for the load transfer:

$$\begin{aligned} \mathbf{u}_\Gamma^f &= \mathbf{M}_{ff}^{-1}\,\mathbf{M}_{fs}\,\mathbf{u}_\Gamma^s \\ \rightarrow \mathbf{f}_\Gamma^s &= \mathbf{M}_{fs}^T\mathbf{M}_{ff}^{-1}\,\mathbf{f}_\Gamma^f = \mathbf{M}_{fs}^T\,\mathbf{p}_\Gamma^f\,, \end{aligned} \qquad (5)$$

which makes this scheme attractive.

2.2 Grid Deformation

Since fluid grid generation is computationally expensive, the fluid grid needs to be deformed to take the new structural displacements into account. Here, the grid is treated as a pseudo-structural system, where the fluid interface displacements are applied as Dirichlet boundary conditions on this system:

$$\begin{bmatrix} \mathbf{K}^f_{\Omega\Omega} & \mathbf{K}^f_{\Omega\Gamma} \\ \mathbf{K}^f_{\Gamma\Omega} & \mathbf{K}^f_{\Gamma\Gamma} \end{bmatrix} \begin{bmatrix} \mathbf{u}^f_{\Omega} \\ \mathbf{u}^f_{\Gamma} \end{bmatrix} = \begin{bmatrix} \mathbf{0} \\ \mathbf{0} \end{bmatrix}. \qquad (6)$$

This equation has to be solved for $\mathbf{u}^f_{\Omega}$ and as an abbreviation the mesh deformation is written as:

$$\mathbf{u}^f = \mathcal{G}\mathbf{u}^f_{\Gamma}, \qquad (7)$$

where $\mathcal{G}$ is the grid deformation operator and $\mathbf{u}^f$ is the whole fluid mesh deformation vector. The stiffness for each finite element is adapted to values depending on the minimal edge legnth. Thus, smaller cells near the wall have a higher stiffness than greater cells in the farfield. Examples of the grid deformation including rigid body motion are depicted in Fig. 3. The matrix $\mathbf{K}$ needs to be evaluated only ones at the beginning of the computation and that here the fluid grid is treated with plane elements rather than the widely used spring analogy [17], which results in high qualitative grids for the fluid solver.

2.3 The fluid solver and the linear stability solver

The Navier-Stokes equations are solved on block-structured grids using an URANS fluid solver which based on a centered finite volume approach [12]. A five stage Runge-Kutta scheme for integration to steady state is utilized. For transient problems the classical second order accurate implicit dual time stepping method is used. An implicit residual smoothing, local time stepping and a multigrid approach is applied for convergence acceleration. Due to the low speed range, a low-Mach number preconditioning is used. The turbulence model was chosen to be the Menter base line (BSL) $k-\omega$ model [18], due to

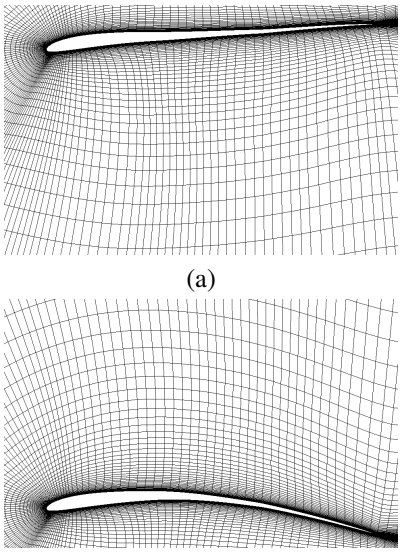

(a)

(b)

Figure 3: Grid deformation

the experience obtained with the SD7003 airfoil [3]. Because the fluid grid changes in every time step due to the grid deformation, the ALE form of the Navier-Stokes equation is solved and the geometric conservation law (GCL) is satisfies within the flow solver. For the coupling scheme, a fluid solver operator $\mathcal{F}$ is introduced as abbreviation, which solves the fluid equations on a given fluid grid configuration to get the fluid force on the interface:

$$\mathbf{f}^f_{\Gamma} = \mathcal{F}\,\mathbf{u}^f. \qquad (8)$$

This fluid solver operator takes also the transition prediction using the e^N-method into account [14, 15]. This method assumes, that the location where the boundary layer breaks down to turbulence corresponds to a certain amplification number of the most unstable Tollmien-Schlichting wave. To calculate the N-factors for the e^N-method, several values of the boundary layer, like the velocity distribution, are transferred from the flow solver to a linear stability solver. The frequencies of all amplified modes are calculated and the amplification region is estimated [19]. For each frequency of an amplified mode the N-factor distribution is calculated and the N-factor curve is obtained by taking the envelope of all N-factor distributions. By comparison of this envelope with a critical N-factor,

the location of transition is found. The challenging point for the partitioned coupling procedure is the fact, that this location needs to be permanently adjusted for the updated grid, which results from the grid deformation step. This critical N-factor can simply be calculated from the given turbulence level of the wind tunnel [20].

Practically, the transition location is calculated along a line from the leading to the trailing edge. Here, this line is the mean line of the airfoil and therefore this line need to be updated before each fluid solver run to consider the deformed grid. Further the transition location is also adapted to the updated grid, which is particularly necessary if the transition is located at the trailing edge.

2.4 Equilibrium Iteration and Time Integration

Due to the use of a partitioned solution procedure, the nonlinear coupled system is solved by an iterative solution procedure. This iteration procedure is also required due to the quasi-incompressible fluid acting on a high-flexible structure, which leads to the so-called added mass effect [21]. Utilizing further a structural solver, which solves the structural equation by the aid of the nonlinear finite element method to get the structural displacements on the interface from prescribed nodal forces:

$$\mathbf{u}_\Gamma^s = \mathcal{S}\mathbf{f}_\Gamma^s \tag{9}$$

the structural displacement residual $\mathbf{r}_{u^s}$ from the current structural displacement vector to an updated one can generally be written as:

$$\mathbf{r}_{u^s} = (\mathcal{S}\circ\mathcal{T}^T\circ\mathcal{F}\circ\mathcal{G}\circ\mathcal{T})\mathbf{u}_\Gamma^s - \mathbf{u}_\Gamma^s. \tag{10}$$

Eq. (10) represents the classical Dirichlet-Neumann step, where the structural interface state is transferred to the fluid side, followed by the grid deformation and solving the fluid problem, followed by the load transfer and solving the structural problem to get a new structural interface state. The residual can be used in a relaxation step (Richardson iteration) to update the

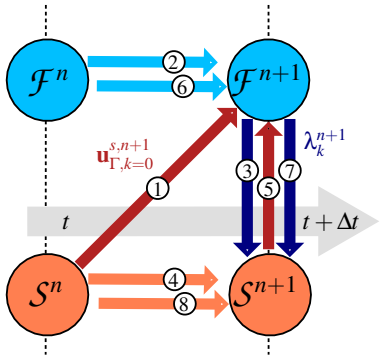

Figure 4: Time integration scheme

structural interface displacements iteratively:

$$\mathbf{u}_{\Gamma,k+1}^s = \mathbf{u}_{\Gamma,k}^s + \omega\mathbf{r}_{u^s}, \tag{11}$$

where ω is the relaxation parameter, which is user-defined.

For transient analysis, the equilibrium iteration described above has to be carried out in every time step to advance the solution from time t to $t+\Delta t$ (time level n to $n+1$). In Fig. 4 a schematic view of the time integration scheme is depicted, while in step 1 a predictor for the next time level is used to reduce the number of iterations [8, 16]. Due to the high nonlinearity of the coupled system, the predicted displacement $\mathbf{u}_{\Gamma,k=0}^{s,n+1}$ is calculated by the aid the structural solver and the load obtained at the time level n:

$$\mathbf{u}_{\Gamma,k=0}^{s,n+1} = \mathcal{S}^{n+1}\mathbf{f}_\Gamma^{s,n}. \tag{12}$$

The data transfer as well as calling of the fluid and structural analysis codes is integrated in a flexible software environment, which provides a user-friendly simulation workspace for the computation of aeroelastic fluid structure interactions [7].

2.5 Computational Domain

The coupled computational grids are shown in Fig. 5. The structural domain is modelled with the aid of layered shell elements to consider the carbon reinforced material. The structure is designed as three overlapping shells and the region of overlapping is incorporated with the aid

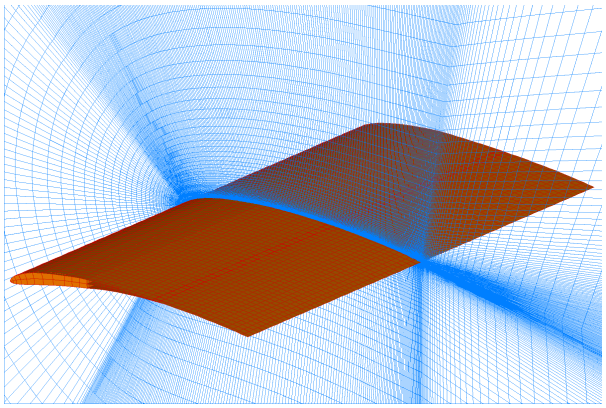

Figure 5: Computational domain

of contact elements [11]. Due to the high flexibility and the contact elements, the structural subdomain needs to be solved with a nonlinear solution scheme. The flapping motion is prescribed at the quarter-chord line and the standard Newmark time integration method is used. The two-dimensional structured fluid grid consists of 585x129 points and the dual time stepping approach is used for time integration.

3 Results

Before the flapping flight motion is investigated, the jig-shape of the airfoil in a steady state flight is calculated. The jig-shape of the airfoil is needed for the design of the structural wind tunnel model. Further the steady state analysis gives a first insight into the principle behavior of the flow field.

3.1 The Airfoil's Jig-Shape

A gliding flight (Reynolds number $Re = 10^5$, angle of attack $\alpha = 3°$) is assumed to obtain the aerodynamic shape of the original airfoil. To get the jig-shape of the airfoil, an iteration process needs to be carried out similar to that of Eq. (10), where the residual is taken as the difference to the original airfoil. The jig-shape is depicted as the black boundary in Fig. 6a. The obtained pressure distribution of the fluid flow around the airfoil is also seen from this figure and the pressure distribution on the airfoil surface is depicted in Fig. 6b. The displacement at the trailing edge is

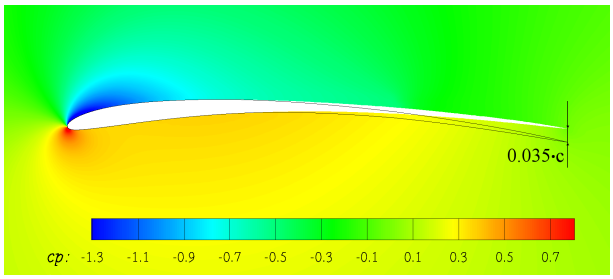

(a) Pressure contours together with the jig-shape of the airfoil

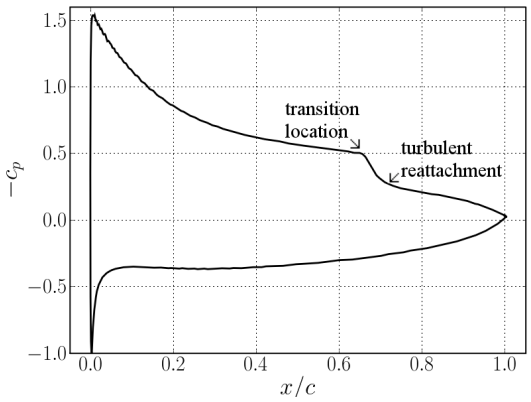

(b) Pressure distribution on the deformed airfoil

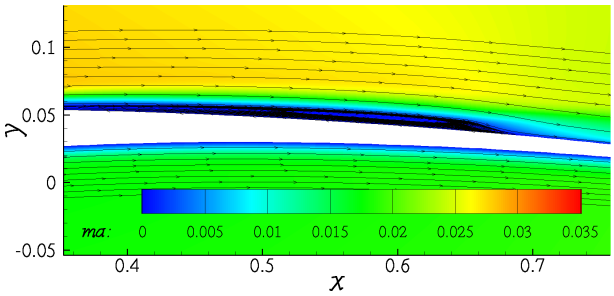

(c) Mach number contours and streamlines

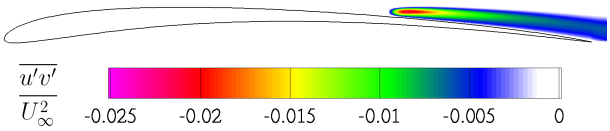

(d) $\overline{u'v'}$-contours

Figure 6: Analysis of the airfoil in gliding flight ($Re = 10^5$, $\alpha = 3°$)

calculated to 3.5% of the chord length. The location of the transition on the upper side of the airfoil is calculated to be at $x_t^u/c = 0.66$. This also can be seen from Fig. 6b, where the transition point is indicated by the pressure rise on the upper surface at this location. The resulting turbulent reattachment occurs at a location 71% of the chord length The Mach number contours are shown in Fig. 6c together with streamlines indicating the laminar separation bubble. The corresponding $\overline{u'v'}$ contours are shown in Fig. 6d. The $\overline{u'v'}$ contours are chosen to be plotted because the turbulent shear stress $\tau = -\rho\overline{u'v'}$ causes transport of momentum across the boundary layer, which is responsible for the closure of the laminar separation bubble. The calculations were carried out with a critical N-factor of $N_{\text{crit}} = 8$, which corresponds to a turbulence level of 0.1%.

3.2 Unsteady calculations

First unsteady computations with pure plunging motion have shown, that the fluid flow shows strong dynamic separations and leading edge vorticities.

Thus, two pitching-plunging motions of the airfoil are investigated here, which differ in their frequency and amplitude. The plunging part of the motion with $z(t)$ being the position of the quarter-chord line can be expressed as:

$$z(t) = \hat{z}\sin(2\pi f t)\,. \tag{13}$$

The effective angle of attack due to the pitching motion is then:

$$\begin{aligned}\alpha_{\text{eff}}(t) &= \alpha(t) + \arctan\left(\frac{\dot{z}(t)}{U_\infty}\right)\\ &= \alpha_0 - \hat{\alpha}\cos(2\pi f t)\\ &\quad + \arctan\left(\frac{2K\hat{z}}{c}\cos(2\pi f t)\right)\\ &\approx \alpha_0 + \left(\frac{2K\hat{z}}{c} - \hat{\alpha}\right)\cdot\cos(2\pi f t)\,,\end{aligned} \tag{14}$$

where the $K = \pi f c/U_\infty$ is the reduced frequency and a phase angle of 90° between the plunging and pitching motion is assumed. Here the following parameters for two cases are used:

- reduced frequency of $K_1 = 0.2$ and $K_2 = 0.4$
- plunging amplitude of $\hat{z}_1 = 0.5c$ and $\hat{z}_2 = 10$ cm
- angle of attack of $\alpha_0 = 4°$
- effective angle of attack amplitude of $\hat{\alpha}_{\text{eff}} = \frac{2K\hat{z}}{c} - \hat{\alpha} = 4°$
- Reynolds number of $Re = 10^5$
- time step size of $\Delta t = \frac{1}{500f}$

The Mach number distribution for the first case (K_1, $\hat{z}_1$) around the airfoil is depicted in Fig. 7a for eight stages of one motion period. The corresponding $\overline{u'v'}$ contours are shown in Fig. 7b. It should be noted here, that periodic results are obtained after two cycles of the prescribed motion and that therefore $2\pi f t$ was set to 0° after two cycles. As can be seen from these pictures, there is a laminar separation bubble on the lower surface side during an angle of $2\pi f t = 0°$. This separation bubble becomes larger and moves slightly to the trailing edge during the upstroke ($2\pi f t = 45°$). Shy before the upper dead center, the separation bubble moves suddenly to the trailing edge and vanishes ($2\pi f t = 90°$). During the downstroke, a new separation bubble appears at the upper trailing edge and becomes larger while traveling fast to the leading edge ($2\pi f t = 135°, 180°, 225°$). While the airfoil moves through the lower dead center, the separation bubble moves to the trailing edge ($2\pi f t = 270°$). During the upstroke, a new separation bubble appears at the lower surface of the airfoil. A similar behavior can be observed for the second case (K_2, $\hat{z}_2$), except that the deformations are higher, Fig. 8.

Further, the time history of the transition position on the lower and upper airfoil side, x_t^u and x_t^l, as well as lift developing is shown in Fig. 9. As observed, the lift produced for the second case with higher plunging amplitude is higher than that for the first case, while the transition location for both cases shows a similar behavior.

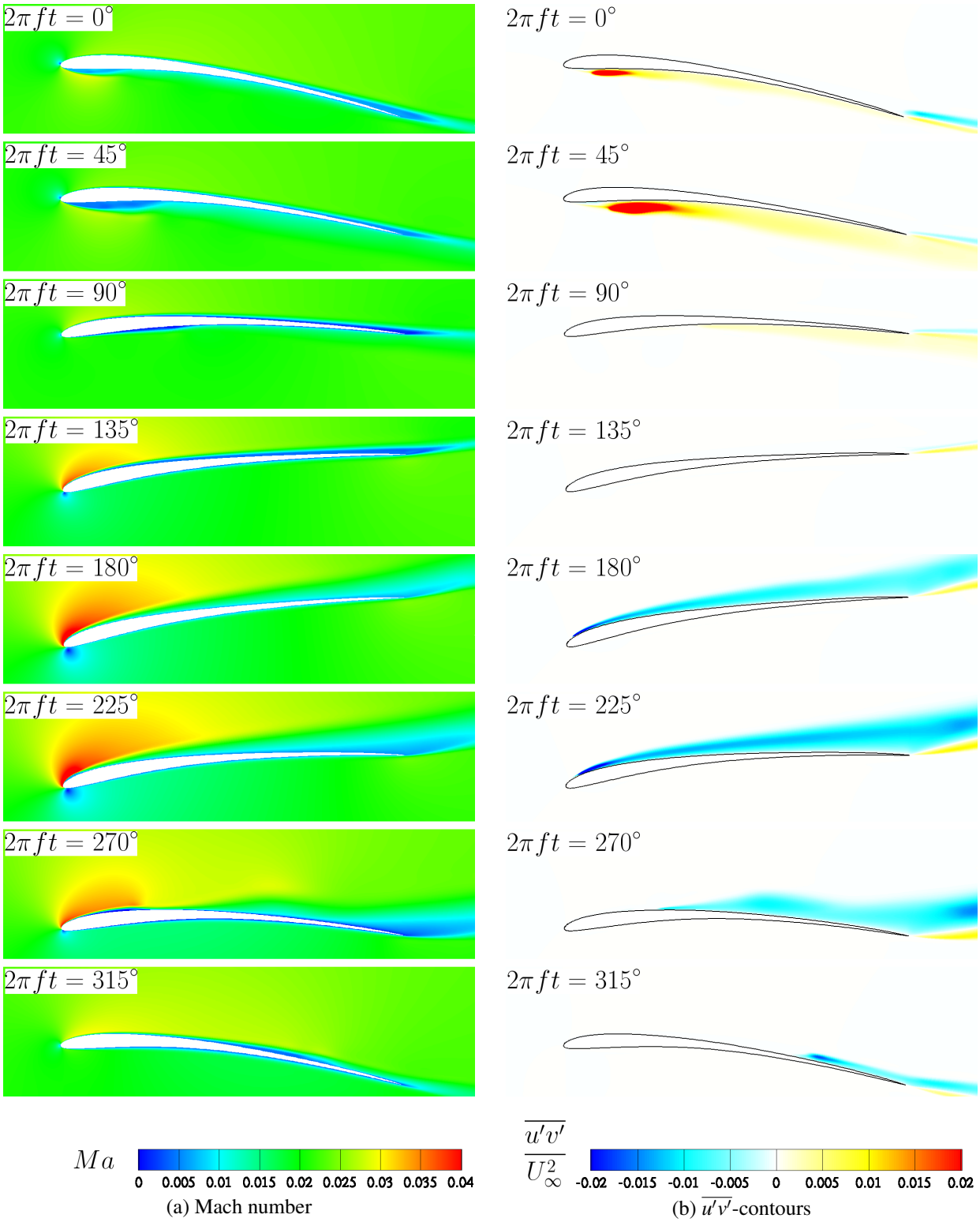

(a) Mach number

(b) $\overline{u'v'}$-contours

Figure 7: Mach number and $\overline{u'v'}$ contours around the airfoil during different motion stages (first case - $K_1 = 0.2$, $\hat{z}_1 = 0.5c$)

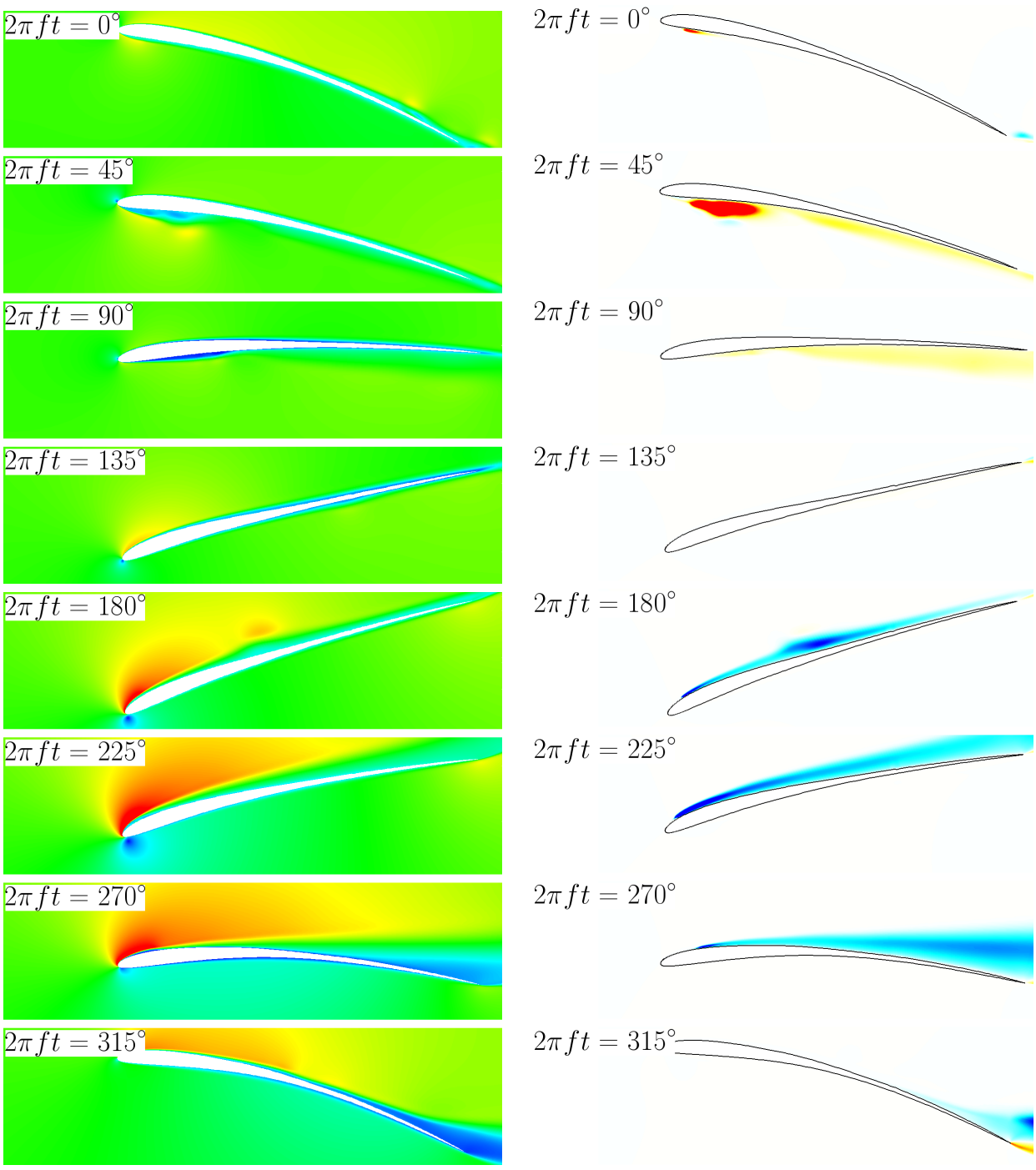

(a) Mach number

(b) $\overline{u'v'}$-contours

Figure 8: Mach number and $\overline{u'v'}$ contours around the airfoil during different motion stages (second case - $K_2 = 0.4$, $\hat{z}_2 = 0.45c$)

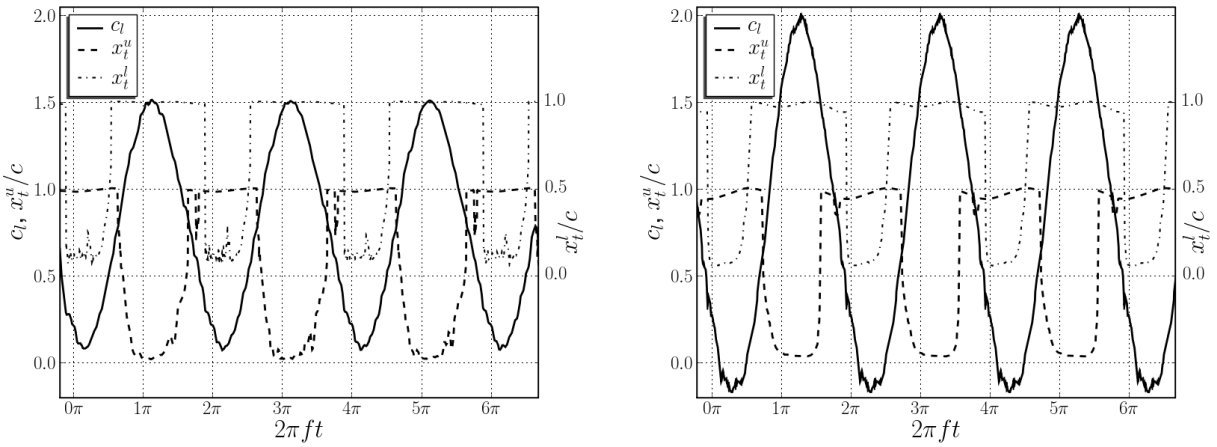

(a) first case - $K_1 = 0.2$, $\hat{z}_1 = 0.5c$)

(b) second case - $K_2 = 0.4$, $\hat{z}_2 = 0.45c$

Figure 9: Time history of lift and transition location over three period

4 Summary

The numerical coupling approach for the multi-disciplinary system has been presented and numerical elements have been discussed. A partitioned coupling procedure has been introduced, which uses a load and energy conservative data transfer scheme and a qualitative grid deformation based on finite elements. Due to the quasi-incompressible fluid and the high-flexible structure, an equilibrium iteration needs to be carried out in every time step. Using a proper predictor, the number of necessary iterations could be reduced considerably. Further, the use of a transition prediction method together with the grid deformation has lead to the need of an automatic adjustment of the transition location for the updated grid.

By calculating the jig-shape of the airfoil for a steady-state flight case, first properties of the flow field could be studied. Here, it has been found, that a laminar separation bubble has formed on the upper side of the airfoil, along those the transition from laminar to turbulent flow takes place. For the unsteady, flapping case, laminar separation bubbles on the upper and lower side of the airfoil move from the trailing edge to the leading and back.

Acknowledgments

The work, presented in this contribution is funded by the German Research Foundation (DFG) as part of the priority program SPP 1207. Further, the authors are deeply grateful for the support of the Institute of Fluid Mechanics regarding the transition prediction module of the fluid solver during the grant period.

References

[1] Lian Y, Shyy W. Laminar-turbulent transition of a low Reynolds number rigid or flexible airfoil. *AIAA Journal*, Vol. 45, pp 1501-1513, 2007.

[2] Yuan W, Khalid M, Windte J, Scholz U, Radespiel R. Computational and experimental investigations of low-Reynolds-number flows past an aerofoil. *The Aeronautical Journal*, Vol. 111, pp 17-29, 2007.

[3] Radespiel R, Windte J, Scholz U. Numerical and experimental flow analysis of moving airfoils with laminar separation bubbles. *AIAA Journal*, Vol. 45, pp 1346-1356, 2007.

[4] Ol M. Comparison of laminar separation bubble measurements on a low Reynolds number airfoil in three facilities. *AIAA-Paper* 2005-5149, 35th AIAA Fluid Dynamics Conference and Exhibit, Toronto, Ontario.

[5] Marxen O, Rist U, Wagner S. Effect of spanwise-modulated disturbances on transition

in a separated boundary layer. AIAA Journal, Vol. 42, pp 937-944, 2004.

[6] Unger R, Haupt MC, Horst P. Application of Lagrange Multipliers for Coupled Problems in Fluid and Structural Interactions. *Computers & Structures*, Vol. 85, pp 796-809, 2007.

[7] Haupt MC, Niesner R, Unger R, Horst P. Coupling techniques for thermal and mechanical fluid-structure-interactions in aeronautics. *PAMM*, Vol. 5, No. 1, pp 19-22, 2005.

[8] Piperno S. Explicit/implicit fluid/structure staggered procedures with a structural predictor and fluid subcycling for 2D inviscid aeroelastic simulations. *Int. J. Num. Meth. Fluids*, Vol. 25, pp 1207-1226, 1997.

[9] Bathe, KJ. *Finite element procedures*. Prentice Hall, Englewood Cliffs, NJ, 1996.

[10] Zienkiewicz OC, Taylor RL. *The Finite Element Method Vol. 1-3*. Butterworth Heinemann, 6th ed., 2005.

[11] Unger R, Haupt MC, Horst P, Windte J. Structural Design and Aeroelastic Analysis of an Oscillating Airfoil for Flapping Wing Propulsion. *AIAA-Paper* 2008-306, 46th AIAA Aerospace Sciences Meeting and Exhibit, Reno, Nevada, 2008.

[12] Blazek, J. *Computational fluid dynamics : principles and applications*. Elsevier, 2007.

[13] Schrauf G. Coast3 – a compressible stability code, user's guide and tutorial. *Technical Report EF 040/98*, Daimler-Benz Aerospace Airbus GmbH, Bremen, 1998.

[14] Smith AMO, Gamberoni N. Transition, pressure gradient, and stability theory. *Report ES 26 388*, Douglas Aircraft, El Segunda, California, 1956.

[15] Stock, HW. Airfoil validation using coupled Navier-Stokes and e^N transition prediction methods. *Journal of Aircraft*, Vol. 39, pp 51-58, 2002.

[16] Unger R., Haupt M.C., Horst P., Coupling Techniques for Computational Nonlinear Transient Aeroelasticity. accepted for publication in *Proceedings of the Institution of Mechanical Engineers Part G – Journal of Aerospace Engineering*, 2008.

[17] Degand C. A three-dimensional torsional spring analogy method for unstructured dynamic meshes. *Computers & Structures*, Vol. 80, pp 305-316, 2002.

[18] Menter FR. Two-equation eddy-viscosity turbulence models for engineering applications. *AIAA Journal*, Vol 32, pp 1598-1605, 1994.

[19] Watmuff, JH. Evolution of a wave packet into vortex loops in a laminar separation bubble. *Journal of Fluid Mechanics*, Vol. 397, pp 119-169, 1999.

[20] Mack, LM. Transition and laminar instability. *Jet Propulsion Laboratory Publication* 77-15, Pasadena, CA, 1977.

[21] Causin P, Gerbeau J-F, Nobile F. Added-mass effect in the design of partitioned algorithms for fluid-structure problems. *Comput. Methods Appl. Mech. Engrg*, Vol. 194, pp 4506-4527, 2005.

Copyright Statement